Journal Pre-proof

A glutathione-responsive photosensitizer with fluorescence resonance energy transfer characteristics for imaging-guided targeting photodynamic therapy

Jing-Jing Cao, Ming-Shan Zhang, Xiao-Qiang Li, De-Chao Yang, Gan Xu, Jian-Yong Liu

PII: S0223-5234(20)30170-7

DOI: https://doi.org/10.1016/j.ejmech.2020.112203

Reference: EJMECH 112203

To appear in: *European Journal of Medicinal Chemistry*

Received Date: 12 December 2019

Revised Date: 1 March 2020

Accepted Date: 1 March 2020

Please cite this article as: J.-J. Cao, M.-S. Zhang, X.-Q. Li, D.-C. Yang, G. Xu, J.-Y. Liu, A glutathione-responsive photosensitizer with fluorescence resonance energy transfer characteristics for imaging-guided targeting photodynamic therapy, *European Journal of Medicinal Chemistry* (2020), doi: https://doi.org/10.1016/j.ejmech.2020.112203.

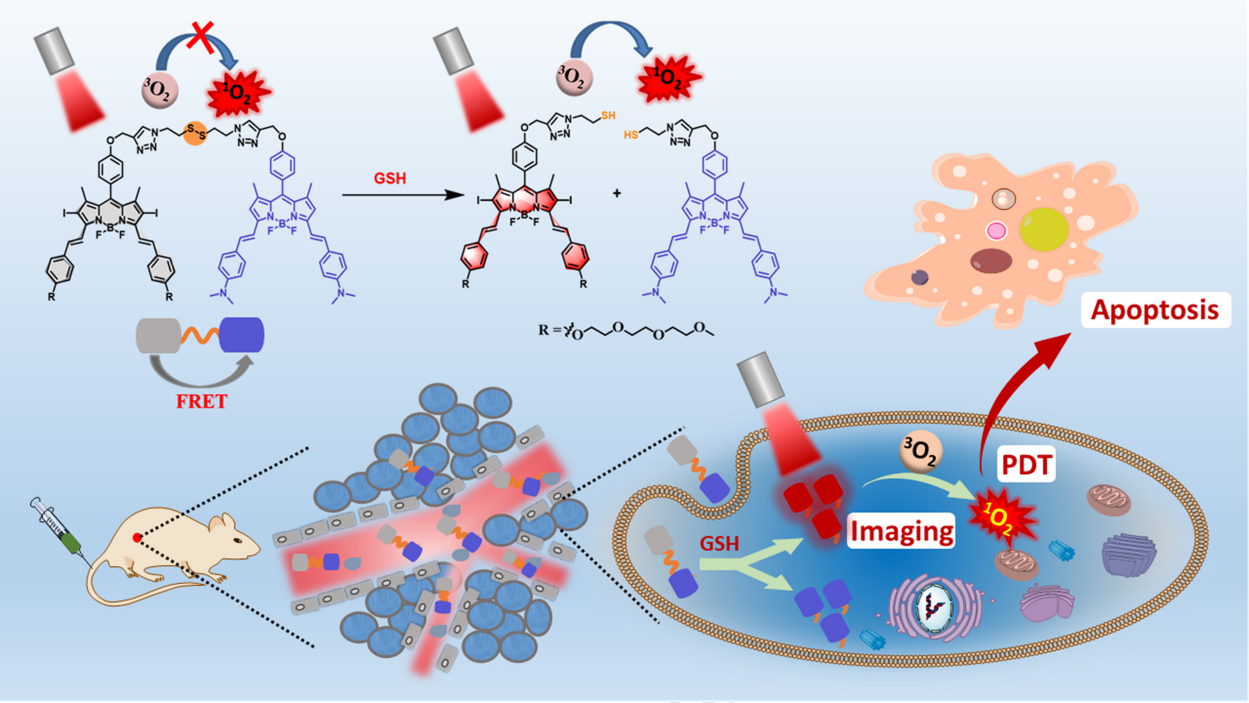

A glutathione-responsive photosensitizer with fluorescence resonance energy transfer characteristics for imaging-guided targeting photodynamic therapy

Jing-Jing Cao [a], Ming-Shan Zhang [a], Xiao-Qiang Li [a], De-Chao Yang [a], Gan Xu [a], Jian-Yong Liu [a, b, c, *]

[a] National & Local Joint Biomedical Engineering Research Center on Photodynamic Technologies, College of Chemistry, Fuzhou University, Fuzhou 350108, China
[b] Key Laboratory of Molecule Synthesis and Function Discovery, Fujian Province University, College of Chemistry, Fuzhou University, Fuzhou 350108, China
[c] State Key Laboratory of Photocatalysis on Energy and Environment, College of Chemistry, Fuzhou University, Fuzhou 350108, China
[*] Correspondence: lkw82@fzu.edu.cn; Tel.: +86-591-22867105

Abstract

Here, we have synthesized and characterized a novel activatable photosensitizer (PS) **8a** in which two well-designed boron dipyrromethene (BODIPY) derivatives are utilized as the photosensitizing fluorophore and quencher respectively, which are connected by a disulfide linker via two successive Cu (I) catalyzed click reactions. The fluorescence emission and singlet oxygen production of **8a** are suppressed via intramolecular fluorescence resonance energy transfer (FRET) from the excited BODIPY-based PS part to quencher unit, but both of them can be simultaneously switched on by cancer-related biothiol glutathione (GSH) in phosphate buffered saline (PBS) solution with 0.05% Tween 80 as a result of cleavage of disulfide. Also, **8a** exhibits a bright fluorescence image and a substantial ROS production in A549 human lung adenocarcinoma, HeLa human cervical carcinoma and H22 mouse hepatoma cells having a relatively high concentration of GSH, thereby leading to a significant photocytotoxicity, with IC_{50} values as low as 0.44 μM, 0.67 μM and 0.48 μM, respectively. In addition, the photosensitizer can be effectively activated and imaged in H22 transplanted hepatoma tumors of mice and shows a strong inhibition on tumor growth. All these results suggest that such a GSH-responsive photosensitizer based on FRET mechanism may provide a new strategy for tumor-targeted and fluorescence imaging-guided cancer therapy.

Keywords

Photodynamic therapy; activatable photosensitizers; GSH-responsive; fluorescence resonance energy transfer (FRET)

1. Introduction

Photodynamic therapy (PDT) utilizes light as the energy source to excite the photosensitizer (PS), then the excited PS reacts with oxygen in tissues inducing the production of reactive oxygen species (ROS), which results in localized cell apoptosis and necrosis. PDT as a new modality, has several distinct advantages over traditional treatments (including chemotherapy, radiotherapy, and surgery) in solid tumors, such as low side effects, minimally invasiveness and negligible multidrug resistance (MDR) [1-3]. However, the clinical use of this treatment is limited by the low cancer selectivity of currently available photosensitizers leading to phototoxicity against normal tissues [4, 5]. To address these problems, there are several commonly used methods. One is conjugation of PS to a targeting ligand, such as biotin [6, 7], folic acid [8, 9], saccharide [10], peptides [11, 12], antibody [13] and tamoxifen [14] etc., which can greatly improve the specificity of PS to tumor tissues. Another is encapsulating the photosensitizers with nanomaterials [15, 16], in which utilizes the enhanced permeability and retention (EPR) effect to achieve passive transport of the photosensitizers to the tumor tissues. Alternatively, activatable photosensitizers are novel but effective agents for selective PDT which have drawn widespread attention in recent years for their unique characteristics [5, 17].

Activatable photosensitizers that mainly based on fluorescence resonance energy transfer (FRET) [18-20], intramolecular charge transfer (ICT) [21, 22], photo-induced electron transfer (PET) [23, 24] and self-quenched mechanisms [25, 26] are in a passive state in normal tissues. However, when going into tumor tissues, with regard to the special microenvironments like hypoxia [27, 28], specific physiological enzymes [29, 30], acidic environment [31, 32] and so on, the photo-physical and photo-chemical properties of which can be restored, including fluorescence emission and photodynamic effect. Considering the significant differences in the concentration

of glutathione (GSH) between the intracellular (~ 10 mM) and the extracellular (~ 2 μM) [33, 34], and the much higher levels in cancer cells than in normal cells [35], GSH-responsive photosensitizers has attracted much attention [36-39].

As a class of versatile fluorescent molecules, boron dipyrromethenes (BODIPYs) have many excellent photo-physical and photo-chemical properties, such as large molar extinction coefficients, high photo-stability and low sensitivity to physiological environment [40, 41]. More importantly, their spectral properties can be finely tuned by modifying the BODIPY core [42], which is beneficial to the design of activatable photosensitizer. In this study, we choose two carefully designed BODIPY derivatives as the photosensitizing fluorophore and quencher respectively, both are linked each other through a disulfide bridge to construct a glutathione-responsive photosensitizer **8a** for near infrared (NIR) fluorescence imaging-guided targeting photodynamic therapy (Scheme 1). Due to intramolecular FRET process between PS and quencher moieties, the activatable PS remains a silent state, as a result, the fluorescence emission, ROS and photodynamic activity can be obviously quenched. However, they will be simultaneously restored when treated with glutathione (Scheme 1). The GSH-responsive properties of this photosensitizer has been validated in vitro as well as in vivo.

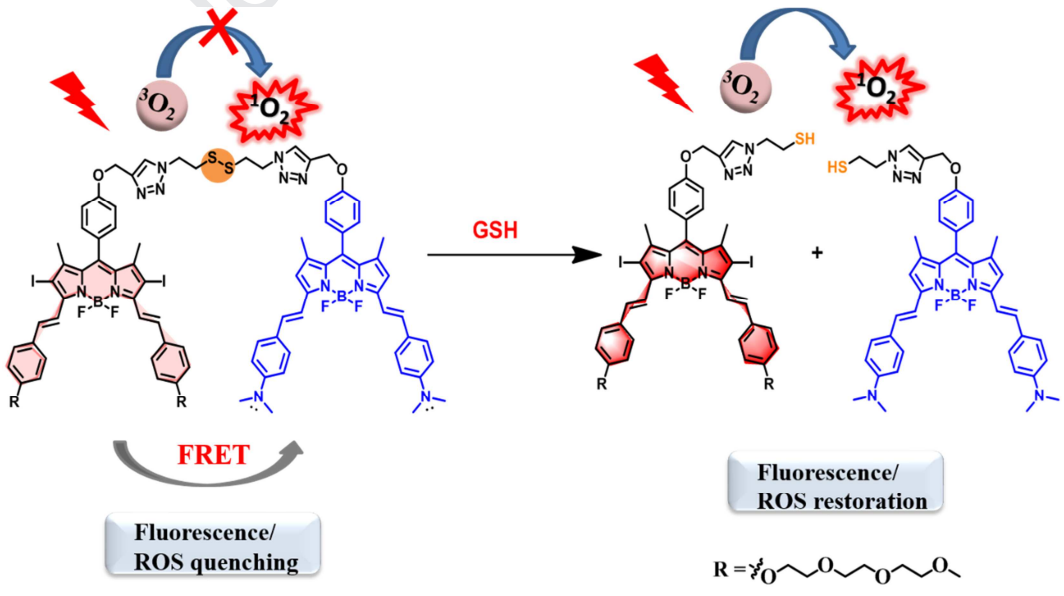

Scheme 1. Schematic illustration of proposed activation mechanism.

2. Results and discussion

2.1. Molecular design and synthesis

The rationally designed GSH-responsive PS includes three modules, a BODIPY-based photosensitizing chromophore, a BODIPY-based quencher and a bio-reducible disulfide linker. Here, BODIPY derivatives are selected as the PS and quencher, which are mainly due to their excellent photo-physical and photo-chemical properties, such as strong absorptions in the visible and near-infrared region (NIR), and high photo-stability. It is noteworthy that their spectral properties can be finely tuned by reasonable chemical modification of the BODIPY core. Fig. 1 shows the detailed synthetic route for the activatable PS **8a**. According to the previously reported procedures, we first synthesized BODIPY **4** [9] being as the photosensitizing agent, the disulfide linker **5a** [43] and BODIPY-based quencher **7** [44]. Both PS **4** and quencher **7** have an alkyne group, they were then linked by diazide **5a** via two successive Cu (I) catalyzed azide-alkyne cycloaddition reactions to afford **8a** with the overall yield of 48%. Two iodine atoms were anchored to the pyrrole rings of BODIPY core, boosting intersystem crossing and singlet oxygen ($^1O_2$) production, made it be an ideal PS. Owing to intramolecular charge transfer (ICT), quencher **7** bearing two *N*,*N*-dimethylamino moieties had a relatively weak fluorescence emission and a red-shift absorption at ca. 705 nm, which well overlapped with the emission of BODIPY **4**. Therefore, upon PS unit was excited, there would be a highly efficient energy transfer in **8a** between the PS and quencher moieties. As a result, the fluorescence emission and $^1O_2$ production were inhibited. When GSH was added, both of them were restored. By contrast, the control group with the non-cleavable C-C linker, **8b**, was also synthesized by employing a similar protocol. Briefly, BODIPY **4** was treated with **5b**, followed by **7** to give **8b** in a moderate yield of 50% (Fig. 1). All the new compounds were purified readily by column chromatography on silica gel and characterized with various spectroscopic methods.

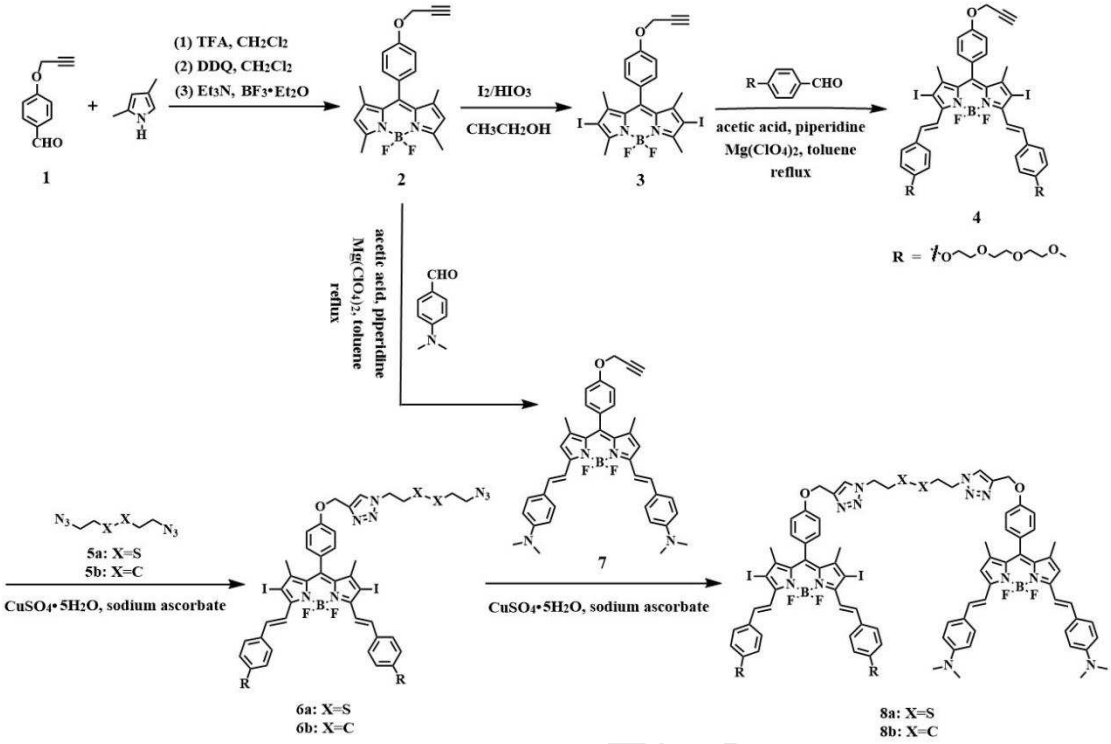

Fig. 1. Synthesis of the GSH-responsive photosensitizer **8a** and the control compound **8b**.

2.2. Spectroscopic and photosensitizing properties

The photo-physical and photo-chemical properties of the target compound **8a** together with the references **8b**, **4** and **7** were measured in both *N*,*N*-dimethylformamide (DMF) and phosphate buffered saline (PBS) solution (pH=7.4, with 0.05% Tween 80), respectively. The results are summarized in Table 1. As shown in Fig. 2, PS **4** had an absorption maximum of 662 nm and fluorescence emission at 620-850 nm in DMF. In particular, this emission was fully covered by the absorption spectra of BODIPY-based quencher **7** (Fig. 2b). Thus, when compound **8a** (or **8b**) was selectively excited at 610 nm, the emission from the quencher moiety around 768 nm (769 nm) was observed while the emission of PS unit at 698 nm (697 nm) was negligible (Fig. 2c), which indicated a highly efficient FRET process was occurred in **8a** (or **8b**) from PS to quencher unit. The fluorescence quantum yield of BODIPY **4** was 0.24 in DMF, while that of the BODIPY donor part of **8a** was significantly reduced to 0.003. So, the quenching efficiency of the aniline-substituted BODIPY in **8a** was

estimated to be 0.99. The singlet oxygen quantum yields of **8a**, **8b** and **4** were also determined by employing 1,3-diphenylisobenzofuran (DPBF) as the indicator and unsubstituted zinc(II) phthalocyanine (ZnPc) as the reference [45]. It could be seen from Table 1 that BODIPY **4** was a highly efficient singlet oxygen generator in DMF and PBS containing 0.05% Tween 80 ($\Phi_\Delta = 0.38$ and 0.30). As expected, after conjugation with the aniline-substituted BODIPY, the products **8a** and **8b** exhibited extremely low Φ_Δ in both DMF and PBS. The pH-responsive properties of **7** and **8a** were then investigated by electronic absorption and fluorescence emission spectra. As shown in Fig. S2 and Fig. S3, both compounds are insensitive to neutral and weakly acidic environment with the pH value higher than 3. So we believe that 8a would not be protonated whether it is in vitro and in vivo experiments.

Table 1. Photo-physical/photo-chemical data of compounds in different solvents.

Solvent	Compounds	λ_{max}^{abs} (nm)	λ_{max}^{em} [a] (nm)	Φ_F [b]	Φ_Δ [c]
DMF	**4**	662	698	0.24	0.38
	7	705	773	0.043	0.007
	8a	664, 704	768	0.052	0.018
	8b	664, 705	769	0.049	0.020
PBS (0.05% Tween 80)	**4**	662	697	0.11	0.30
	7	708	744	0.014	0.006
	8a	668, 709	742	0.021	0.015
	8b	669, 708	744	0.019	0.016

[a] Excited at 610 nm; [b] Relative to unsubstituted zinc(II) phthalocyanine (ZnPc) in DMF as the reference (Φ_F = 0.28). [c] Relative to unsubstituted zinc(II) phthalocyanine (ZnPc) in DMF as the reference (Φ_Δ = 0.56).

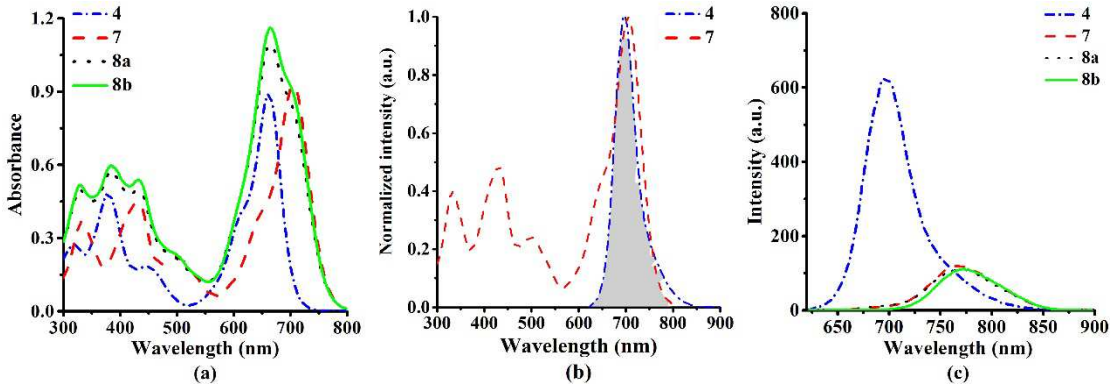

Fig. 2. (a) UV-Vis absorption spectra of **4** (–·–), **7** (– –), **8a** (· · ·) and **8b** (—) (all at 10 μM) in DMF; (b) Overlaps between the fluorescence spectrum (λ_{ex} = 610 nm) of PS **4** (–·–) and the absorption spectrum of quencher **7** (– –) in DMF and (c) fluorescence emission spectra (λ_{ex} = 610 nm) of **4** (–·–), **7** (– –), **8a** (· · ·) and **8b** (—) (all at 10 μM) in DMF.

The activation of **8a** by GSH was examined by monitoring its spectral changes in PBS solution containing 0.05% Tween 80. Here, we set the GSH concentrations to 2 μM and 10 mM, which simulates the extracellular and intracellular bio-distribution of glutathione respectively. As shown in Fig. 3a and Fig. S4, when 2 μM GSH was added, even if incubated for 720 min in PBS with 0.05% Tween 80, the changes in fluorescence of **8a** at 698 nm were negligible. However, when 10 mM GSH was added, the fluorescence of **8a** at 698 nm was steadily enhanced with the culture time. After co-culture for 720 min, the fluorescence quantum yield of **8a** from BODIPY photosensitizer was recovered to be 0.085. Given that the fluorescence quantum yield of compound **4** in PBS was 0.11, 77% of **8a** was estimated to be cleaved by 10 mM GSH for 720 min. This process followed pseudo-first-order kinetics with $k_{obs} = 5.8 \times 10^{-3}$ min^{-1} for **8a** (Fig. S5). These results suggested that the disulfide bond of **8a** could be efficiently cleaved resulting in fluorescence restoration of BODIPY-based PS by a millimolar concentration of GSH, but not a micromolar concentration of GSH. It means that compound **8a** can keep stable in a quenched state during blood circulation, but upon it enters into cancer cells, will be activated by intracellular GSH. In addition, we also investigated the control group and found that the fluorescence intensity of **8b** remained almost unchanged regardless of the amount of GSH added.

The ability of **8a** and **8b** to produce $^1O_2$ was also explored in PBS solution with 0.05% Tween 80 by using 9,10-dimethylanthracence (DMA) as the $^1O_2$ scavenger. DMA can be decomposed by $^1O_2$ from PS under light illumination. As a result, the fluorescence emission of DMA at 432 nm was vanished. As depicted in Fig. 3b and Fig. S6, there was not obvious changes for fluorescence of DMA at 432 nm in the presence of **8a** and **8b** under irradiation at 670 nm, which indicated both **8a** and **8b** couldn't effectively generate singlet oxygen. However, treated **8a** with millimolar concentration of glutathione, the fluorescence of DMA at 432 nm decreased dramatically (Fig. 3b and Fig. S6). This was because that **8a** was activated by GSH to generate $^1O_2$ inducing degradation of DMA. And **8a** treated with GSH (10 mM) exhibited a slight lower $^1O_2$ generation efficiency than the reference BODIPY **4**. Besides, there was no chance to

activate the reference compound **8b** with the non-cleavable linker by using any concentration of GSH. In brief, the intramolecular FRET process in **8a** quenches most of their singlet excited state, reducing the fluorescence emission and singlet oxygen generation efficiency, and the glutathione with millimolar concentration can activate them.

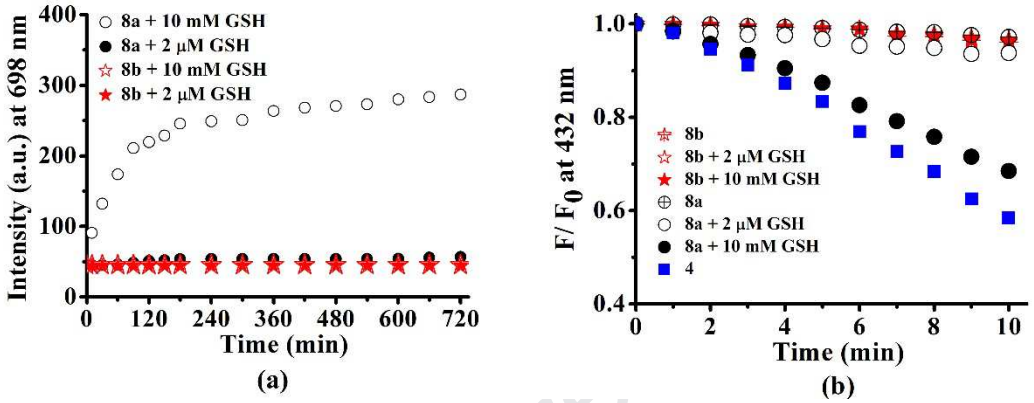

Fig. 3. (a) Changes in the fluorescence intensity of **8a** (10 μM) and **8b** (10 μM) at 698 nm in PBS with 0.05% Tween 80 in the presence of GSH (2 μM and 10 mM, respectively); (b) Comparison of the degradation rates of DMA in PBS with 0.05% Tween 80 as monitored by the decrease in fluorescence intensity at 432 nm with irradiation time both using **8a** and **8b** as the photosensitizers (both at 10 μM) in the presence of GSH (2 μM and 10 mM, respectively).

2.3. In vitro studies

To study the activation of **8a** at cellular level, we first investigated the fluorescence imaging by incubating this dye with HeLa, A549 and H22 cancer cells as well as HELF human embryonic lung fibroblast cells. As demonstrated in Fig. 4, when treatment of HeLa, A549 and H22 cells with **8a** (10 μM) for 8 h, a bright intracellular fluorescence was observed. The results indicated that **8a** could be well uptaken by the three cancer cells, and then efficiently activated by intracellular biothiols. By contrast, the fluorescence in HELF normal cells with a lower concentration of GSH was much weaker than that in the three cancer cells. On the other hand, these four cells pretreated with exogenous GSH (5 mM) for 2 h and followed by **8a** for another 8 h, the intracellular fluorescence intensity dramatically increased. These results suggested that **8a** remained in a quenched state in normal cells, but could be activated by biothiols of higher concentration in cancer cells, thereby leading to an enhanced fluorescence

emission. Besides, for the non-cleavable analogue **8b,** no matter whether pre-treated with GSH or not, there was almost negligible fluorescence in all the four cell lines. And the same conclusion can be reached from flow cytometry analysis (Fig. S7).

To account for the different activated behaviors of **8a** between the cancer and normal cell lines, we investigated the intracellular GSH concentrations in HeLa, A549, H22 and HELF cells with Total Glutathione Assay Kit (Fig. S8). It could be seen that the GSH levels in HeLa, A549 and H22 cancer cells were much higher than that in HELF normal cells, which well explained the higher activation of **8a** in the three cancer cells.

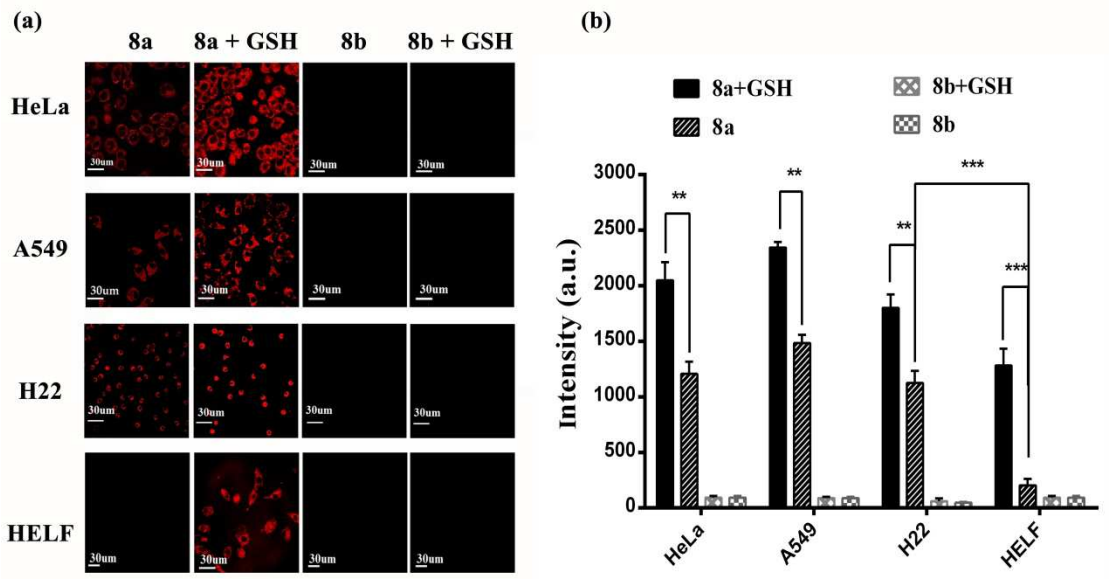

Fig. 4. (a) Confocal laser scanning microscopy (CLSM) images of HeLa, A549, H22 and HELF cells after incubation with **8a** (or **8b**) (10 μM) for 8 h, or cells pre-treated with GSH (5 mM) for 2 h, followed by treatment of **8a** (or **8b**) (10 μM) for another 8 h; (b) quantitative results of (a) (** $p < 0.01$, *** $p < 0.001$).

Reactive oxygen species (ROS) is an important factor in PDT. Next, we examined intracellular ROS levels of **8a** and **8b** in HeLa, A549, H22 and HELF cells under light irradiation by using 2',7'-dichlorofluorescein diacetate (DCFH-DA) as the ROS probe. DCFH-DA itself does not emit fluorescence, but its oxidized product DCF by ROS is highly fluorescent. Therefore, the ROS level in living cells can be determined by monitoring intracellular DCF fluorescence. As shown in Fig. 5, a substantial green fluorescence of DCF in the green channel and a strong red fluorescence of PS in the red

channel were observed when the A549 cells were illuminated by NIR light after treatment with **8a** for 12 h. It was believed that the intracellular thiols could cleaved **8a**, which led to a turn-on fluorescence emission accompanying by a substantial ROS. Moreover, the intracellular fluorescence in both green and red channels was found to be stronger when the A549 cells were pretreated with exogenous GSH (5 mM), followed by **8a**, which indicated exogenous GSH promoted the release of PS, thereby elevating the intracellular ROS level. When Vitamin C (VC) (100 μM), a ROS inhibitor, was added, the green fluorescence of DCF substantially decreased, but there was not obvious change in fluorescence intensity of **8a**. This is because the ROS produced by activated **8a** was heavy eliminated by VC, resulting in a reduced DCF fluorescence emission. The same experiment results were demonstrated in HeLa and H22 cells (Fig. S9 and Fig. S10). In contrast, negligible fluorescence in both channels was observed in HELF cells and the exogenous GSH can promote the intracellular fluorescence emission and ROS production. For the control **8b**, the fluorescence in both channels was few captured for all the four cell lines in any cases.

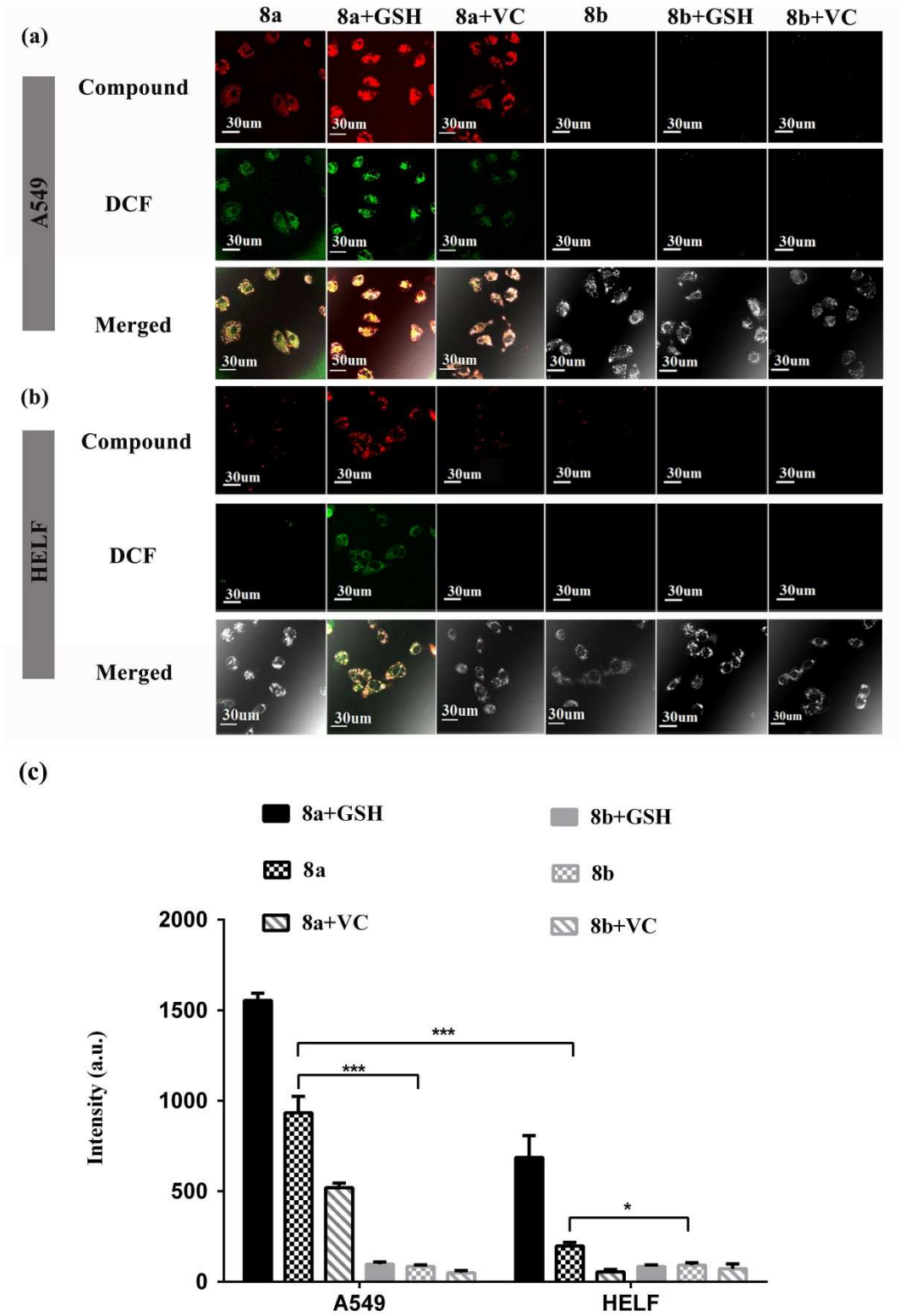

Fig. 5. CLSM images of (a) A549 and (b) HELF cells incubated with **8a** (or **8b**) (10 μM) for 12 h, pretreated with GSH (5 mM) for 2 h and then incubated with **8a** (or **8b**) (10 μM) for another 12 h or pretreated with VC (100 μM) for 1 h and then incubated with **8a** (or **8b**) (10 μM) for another 12 h. The green fluorescence is DCF signals, the red fluorescence is PS signals; (c) quantitative results of DCF green fluorescence in (a) and (b) (* $p < 0.05$, ** $p < 0.01$, *** $p < 0.001$).

In addition, the cytotoxicity of **8a** and **8b** was evaluated by MTT assay in HeLa, A549, H22 and HELF cells. The results were described in Fig. 6. Compound **8a** was basically noncytotoxic against all the four cell lines up to 10 μM without light. However, once exposed to light (λ = 670 nm, 20 mW·cm^{-2}, 2.4 J· cm^{-2}), it was found that there was a high cytotoxicity to HeLa, A549 and H22 cancer cells, but not HELF normal cells. The IC_{50} values, defined as the drug concentrations required to kill 50% of the cells, are as low as 0.67 μM (for HeLa cells), 0.44 μM (for A549 cells) and 0.48 μM (for H22 cells), respectively. While, the reference **8b** showed few toxicity to any cells in the absence or in the presence of light. It was concluded that **8a** could selectively be activated in cancer cells with relatively high biological thiols leading to a specific attack to cancer cells.

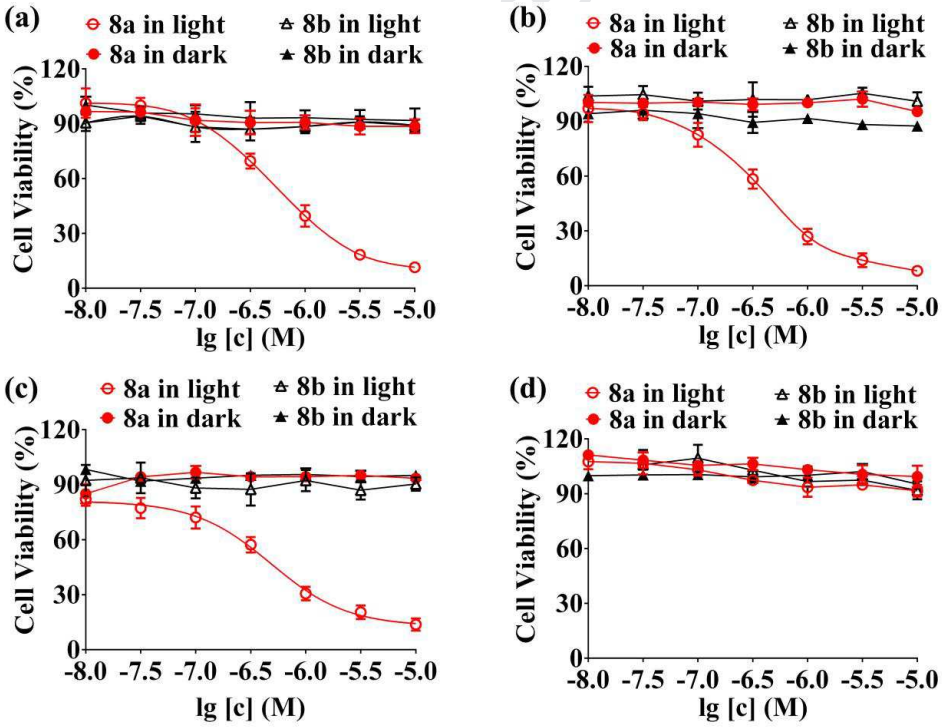

Fig. 6. Cytotoxic effects of **8a** (circles) and **8b** (triangles) against (a) HeLa, (b) A549, (c) H22 and (d) HELF cells in the absence (closed symbols) and presence (open symbols) of light (λ = 670 nm, 20 mW·cm^{-2}, 2.4 J· cm^{-2}). Data are expressed as the mean value ± standard error of the means of three independent experiments, each performed in sextuplicate.

To ascertain the distribution of PS in cellular organisms, the subcellular localization of **8a** was also studied in HeLa, A549 and H22 cells (Fig. 7, Fig. S11, Fig.

S12). The cells were first cultured with **8a**, then stained with DAPI, Mito-Tracker Green and Lyso-Tracker Red which are specific fluorescence probes for nucleus, mitochondria and lysosomes, respectively. Finally, the intracellular fluorescence images of PS and probes were captured via two different channels by confocal laser scanning microscopy (CLSM). As demonstrated in Fig. 7a, the fluorescence of Mito-Tracker and **8a** were well superimposed. And the line traces in the last column also illustrated this conclusion. In addition, the experimental results in lysosomes were similar to those of mitochondria (Fig. 7b). By contrast, the fluorescence images of **8a** and the DAPI could not be superimposed well (Fig. 7c). All above suggested that GSH-mediated cleavage of **8a** could occur in mitochondria and lysosomes.

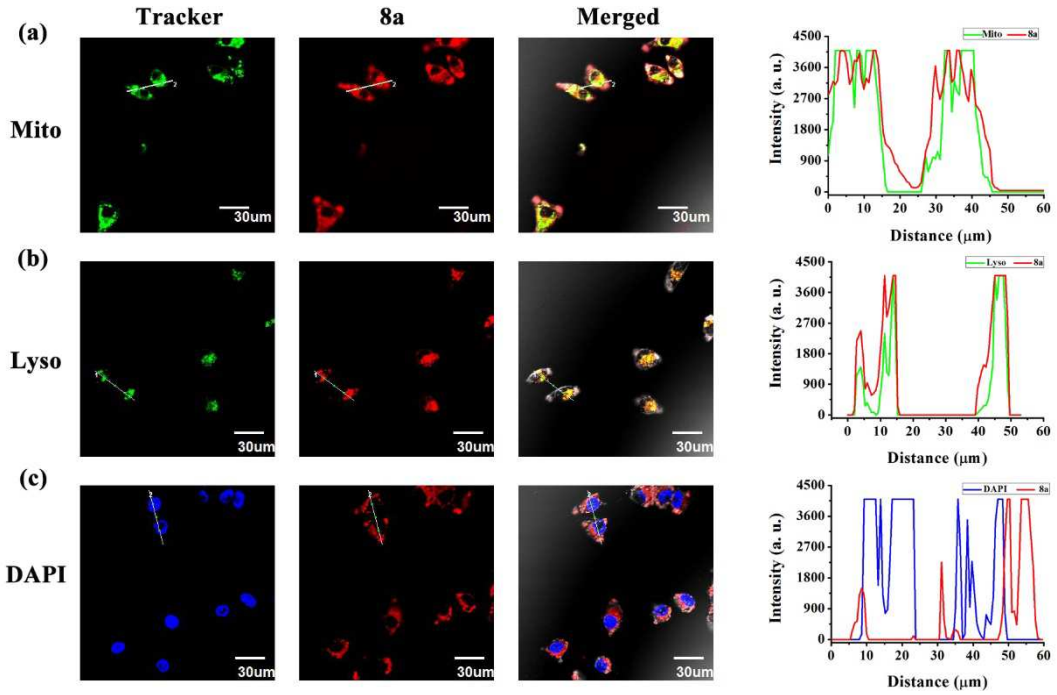

Fig. 7. Visualization of the intracellular fluorescence of A549 cells for Mito-Tracker (in green, a), Lyso-Tracker (in green, b) and DAPI (in blue, c). The last column is fluorescence intensity profiles of Mito-Tracker, Lyso-Tracker, DAPI and **8a** (10 μM) traced along the white line in (a, b, c).

2.4. In vivo study

To further confirm the activation of **8a** in solid tumors, the in vivo fluorescence imaging was performed on H22 tumor-bearing mice by fluorescence molecular tomography (FMT) using the FMT^{TM} 2500 system (PerkinElmer Inc.). As shown in

Fig. 8a, the apparent fluorescence signals in tumor were observed for mouse after administration with **8a** (2 mg/kg, 200 μL) via tail-intravenous injection for 2 h and the signal intensity increased along with time, implying that **8a** could be efficiently accumulated and activated in tumor tissues. While, the signals in the surrounding normal tissues were insignificant, which might be due to low accumulation or poor activation of **8a** in these area. In comparison, for the control **8b**, significantly weak fluorescence signals were captured in the whole body including tumor tissues as a result of non-cleavable linker. The same experimental phenomenon was observed in the ex vivo fluorescence imaging for the harvested tumor and major organs (heart, liver, spleen, lung and kidney) (Fig. 8b).

Encouraged by the above results, next, we assessed the in vivo photodynamic effects of **8a** by using H22 tumor-bearing mice. They were randomly divided into five groups treated with saline, **8a**, **8a**+light, **8b** and **8b**+light, respectively. It was found that for the saline control group after 15 days administration, there was a fast tumor growth which could be reflected by the huge changes in tumor sizes (Fig. 9b). Similar results were obtained for the groups treated with only **8a** or **8b** without light suggesting negligible dark toxicity. After laser irradiation, **8a** exhibited a significant inhibition for tumor growth. Comparatively, only a slight tumor growth inhibition was achieved for the mice treated with **8b**+light. The excellent photodynamic antitumor performance of **8a** was also verified by the average tumor weights (Fig. 9c) and tumor photographs (Fig. 9d). In order to further confirm in vivo anti-tumor effect, tumors were excised and subjected to histological analysis via hematoxylin and eosin (H&E) staining assay. A high level of cell necrosis and apoptosis was observed in the **8a**+light treated tumor tissues, which was indiscernible for the mice receiving the other four treatments (Fig. 10).

Considering biosafety, we simultaneously monitored the body weights of all the mice every day during the treatment (Fig. 9a), as illustrated there were no abnormal changes among all the groups after injection during 15 days, which demonstrated good

biocompatibility and low bio-toxicity of **8a** and **8b**. Moreover, the H&E staining images (Fig. S13) for the major organs (heart, liver, spleen, lung, and kidney) in the mice treated with **8a**+light and **8b**+light further manifested no systemic toxicity of **8a** and **8b**. All the results indicate that **8a** can be served as a promising fluorescence imaging-guided targeting antitumor PS.

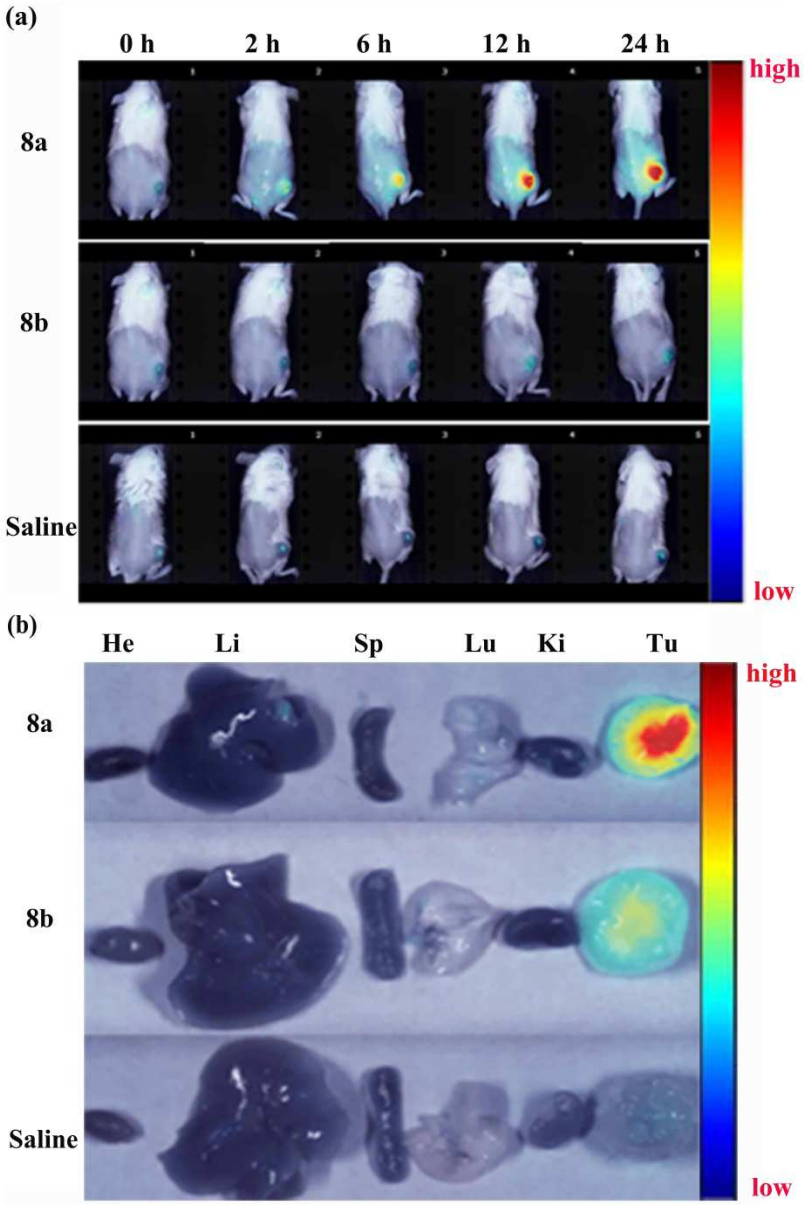

Fig. 8. (a) In vivo fluorescence images of mice bearing H22 hepatocellular tumor taken at different time after intravenous injection of **8a**, **8b** and saline; (b) Ex vivo images of the different organs of mice, including kidney, lung, spleen, liver, heart, and tumor, which were sacrificed at 24 h after injection (He: heart; Li: liver; Sp: spleen; Lu: lung; Ki: kidney; Tu: tumor).

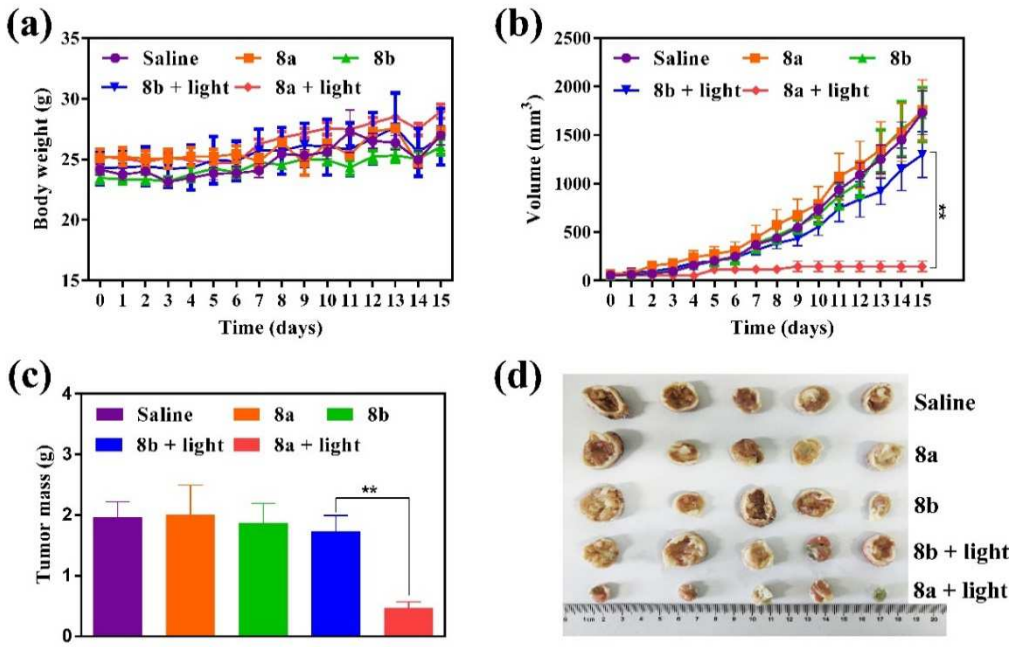

Fig. 9. (a) Changes in body weight; (b) Changes in tumor volume; (c) Mean tumor mass; (d) Photograph of the excised tumors, after treatment with **8a**, **8b**, **8a**+light, **8b**+light and saline. Data are expressed as the mean value ± standard error of the means of three independent experiments, (* $p < 0.05$, ** $p < 0.01$, *** $p < 0.001$).

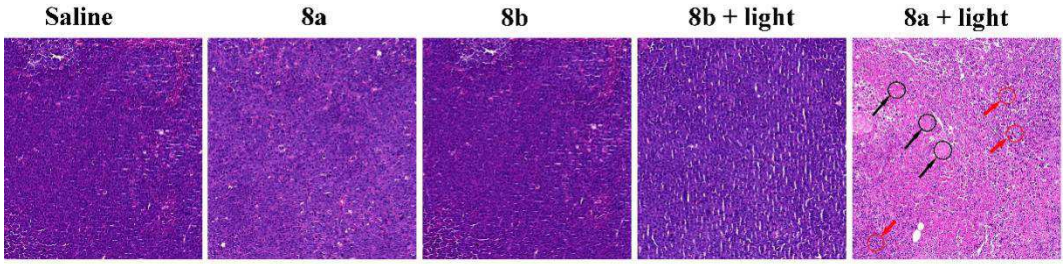

Fig.10. H&E staining images of tumors for different groups after 15 days treatment. Red arrows represent areas of apoptosis and black arrows are areas of necrosis.

3. Conclusions

In summary, a novel GSH-responsive NIR PS based on FRET mechanism has been synthesized and characterized. This PS can be activated by exogenously added GSH with a concentration of millimolar in PBS solution with 0.05% Tween 80, and endogenous biothiol in the A549, HeLa and H22 cancer cells companying with significant fluorescence emission, high ROS production, and photodynamic effect. The in vivo studies for H22 tumor-bearing mice demonstrate a strong tumor-imaging and a substantial tumor growth inhibition ability of **8a** with good biosafety. All results strongly indicate that this kind of GSH-responsive photosensitizer has a great potential for tumor-targeted and fluorescence imaging-guided cancer therapy.

4. Experimental

4.1. Genernal

Experimental details regarding the purification of solvents, instrumentation and synthesis of compounds **1-5** and **7** presented in electronic supplementary information.

*4.1.1. Synthesis of **6a***

A mixture of **4** (50 mg, 44 μmol) and **5a** (41 mg, 200 μmol) in dichloromethane (6 mL) was added to a solution of $CuSO_4 \cdot 5H_2O$ (10 mg, 40 μmol) and sodium ascorbate (30 mg, 150 μmol) in a 1:1 mixture of water and ethanol (1 mL). The mixture was stirred at room temperature overnight, and then was poured into water (20 mL), extracted with dichloromethane three times (3×20 mL). The crude product was further purified by column chromatography on silica gel using CH_2Cl_2/CH_3OH (30:1, v/v) as the eluent to give **6a** as a green solid (36 mg, 67%). ^{1}H NMR (400 MHz, $CDCl_3$): δ = 8.13 (d, *J* = 16.4 Hz, 2 H, CH=CH), 7.75 (s, 1 H, triazole-H), 7.60 (d, *J* = 8.4 Hz, 4 H, ArH), 7.58 (d, *J* = 16.4 Hz, 2 H, CH=CH), 7.19 (d, *J* = 8.4 Hz, 2 H, ArH), 7.14 (d, *J* = 8.4 Hz, 2 H, ArH), 6.96 (d, *J* = 8.4 Hz, 4 H, ArH), 5.29 (s, 2 H, OCH_2), 4.74 (t, *J* = 6.4 Hz, 2 H, NCH_2), 4.19 (t, *J* = 4.8 Hz, 4 H, OCH_2), 3.89 (t, *J* = 4.8 Hz, 4 H, OCH_2), 3.78-3.74 (m, 4 H, OCH_2), 3.72-3.65 (m, 8 H, OCH_2), 3.61 (t, *J* = 6.4 Hz, 2 H, CH_2N_3), 3.58-3.54 (m, 4 H, OCH_2), 3.38 (s, 6 H, OCH_3), 3.21 (t, *J* = 6.4 Hz, 2 H, SCH_2), 2.90 (t, *J* = 6.4 Hz, 2 H, SCH_2), 1.49 (s, 6 H, CH_3); ^{13}C NMR (150.7 MHz, $CDCl_3$) δ: 159.95, 159.16, 150.42, 145.66, 143.52, 139.08, 138.30, 133.20, 129.74, 129.69, 129.24, 127.93, 123.69, 116.74, 115.69, 114.98, 82.70, 71.93, 70.87, 70.65, 70.57, 69.67, 67.54, 62.02, 59.05, 49.84, 48.81, 37.70, 37.52, 17.71 ppm; HRMS (ESI): m/z calcd for $C_{54}H_{63}BF_2I_2N_8NaO_9S_2$: 1357.2202 $[M+Na]^+$; found 1357.2205.

*4.1.2. Synthesis of **6b***

According to the above procedure, **4** (50 mg, 44 μmol) was treated with **5b** (40 mg, 210 μmol) in the presence of $CuSO_4 \cdot 5H_2O$ (10 mg, 40 μmol) and sodium ascorbate (30 mg, 150 μmol) to give **6b** as a green solid (34 mg, 73%). ^{1}H NMR (400 MHz, $CDCl_3$): δ = 8.13 (d, *J* = 16.8 Hz, 2 H, CH=CH), 7.66 (s, 1 H, triazole-H), 7.60 (d, *J* = 7.6 Hz, 4

H, ArH), 7.58 (d, *J* = 16.8 Hz, 2 H, CH=CH), 7.19 (d, *J* = 7.6 Hz, 2 H, ArH), 7.14 (d, *J* = 7.6 Hz, 2 H, ArH), 6.96 (d, *J* = 7.6 Hz, 4 H, ArH), 5.28 (s, 2 H, OCH_2), 4.40 (t, *J* = 6.8 Hz, 2 H, NCH_2), 4.22-4.16 (m, 4 H, OCH_2), 3.92-3.86 (m, 4 H, OCH_2), 3.78-3.73 (m, 4 Hz, OCH_2), 3.72-3.64 (m, 8 H, OCH_2), 3.59-3.53 (m, 4 H, OCH_2), 3.39 (s, 6 H, OCH_3), 3.28 (t, *J* = 6.8 Hz, 2 H, CH_2N_3), 2.01-1.92 (m, 2 H, CH_2), 1.65-1.56 (m, 2 H, CH_2), 1.49 (s, 6 H, CH_3), 1.46-1.36 (m, 4 H, CH_2); ^{13}C NMR (150.7 MHz, $CDCl_3$) δ: 160.09, 159.33, 150.58, 145.78, 143.67, 139.24, 138.44, 133.34, 129.89, 129.86, 129.39, 128.06, 122.82, 116.90, 115.84, 115.13, 82.84, 72.07, 71.01, 70.80, 70.71, 69.82, 67.69, 62.26, 59.20, 51.37, 50.47, 30.32, 28.78, 26.30, 26.21, 17.83 ppm; HRMS (ESI): m/z calcd for $C_{56}H_{67}BF_2I_2N_8NaO_9$: 1321.3074 $[M+Na]^+$; found 1321.3076.

*4.1.3. Synthesis of GSH-responsive PS **8a***

According to the procedure for **6a**, treatment of **7** (26 mg, 41 μmol) with **6a** (50 mg, 38 μmol), $CuSO_4 \cdot 5H_2O$ (10 mg, 40 μmol) and sodium ascorbate (30 mg, 150 μmol) afforded **8a** as a green solid (55 mg, 71%). ^{1}H NMR (400 MHz, pyridine-d_5): δ = 8.54 (d, *J* = 16.4 Hz, 2 H, CH=CH), 8.40 (s, 1 H, triazole-H), 8.38 (s, 1 H, triazole-H), 8.28 (d, *J* = 16.0 Hz, 2 H, CH=CH), 8.19 (d, *J* = 16.4 Hz, 2 H, CH=CH), 7.74 (d, *J* = 8.4 Hz, 4 H, ArH), 7.68 (d, *J* = 8.8 Hz, 4 H, ArH), 7.64 (d, *J* = 16.4 Hz, 2 H, CH=CH), 7.42 (d, *J* = 8.4 Hz, 2 H, ArH), 7.35 (d, *J* = 8.4 Hz, 2 H, ArH), 7.33 (d, *J* = 8.4 Hz, 2 H, ArH), 7.21 (d, *J* = 8.4 Hz, 2 H, ArH), 6.99 (d, *J* = 8.8 Hz, 4 H, ArH), 6.85 (s, 2 H, pyrrole-H), 6.63 (d, *J* = 8.8 Hz, 4 H, ArH), 5.54 (s, 2 H, OCH_2), 5.50 (s, 2 H, OCH_2), 4.90-4.84 (m, 4 H, NCH_2), 4.16 (t, *J* = 4.4 Hz, 4 H, OCH_2), 3.83 (t, *J* = 4.8 Hz, 4 H, OCH_2), 3.74-3.70 (m, 4 H, OCH_2), 3.70-3.64 (m, 8 H, OCH_2), 3.54 (t, *J* = 4.8 Hz, 4 H, OCH_2), 3.39 (t, *J* = 5.6 Hz, 4 H, SCH_2), 3.37 (t, *J* = 5.6 Hz, 4 H, SCH_2), 3.29 (s, 6 H, OCH_3), 2.77 (s, 12 H, NCH_3), 1.55 (s, 6 H, CH_3), 1.54 (s, 6 H, CH_3); ^{13}C NMR (150.7 MHz, $CDCl_3$): δ = 160.08, 159.27, 158.69, 152.84, 160.00, 150.49, 145.78, 143.90, 143.62, 140.98, 139.18, 138.47, 136.56, 133.30, 130.18, 130.03, 130.00, 129.84, 129.80, 129.34, 129.18, 128.38, 127.92, 125.10, 123.93, 123.78, 117.38, 116.86, 115.83, 115.34, 115.11, 114.92, 112.23, 82.82, 72.05, 70.98, 70.77, 70.69, 69.79, 67.67, 61.99, 59.16, 48.83, 40.36, 37.92, 37.80, 17.82, 14.95; HRMS (ESI): *m/z* calcd for

$C_{94}H_{103}B_2F_4I_2N_{12}O_{10}S_2$ $[M+H]^+$, 1975.5568, found, 1975.5582.

*4.1.4. Synthesis of reference **8b***

According to the procedure for **6a**, treatment of **7** (26 mg, 41 μmol) with **6b** (52 mg, 39 μmol), $CuSO_4 \cdot 5H_2O$ (10 mg, 40 μmol) and sodium ascorbate (30 mg, 150 μmol) afforded **8b** as a green solid (52 mg, 68%). ^{1}H NMR (400 MHz, $CDCl_3$): δ = 8.13 (d, *J* = 16.4 Hz, 2 H, CH=CH), 7.63-7.57 (m, 8 H, CH=CH and triazole-H and ArH), 7.55 (d, *J* = 16.4 Hz, 2 H, CH=CH), 7.51 (d, *J* = 8.4 Hz, 4 H, ArH), 7.21-7.14 (m, 4 H, CH=CH and ArH), 7.13-7.09 (m, 4 H, ArH), 7.06 (d, *J* = 7.6 Hz, 2 H, ArH), 6.95 (d, *J* = 8.0 Hz, 4 H, ArH), 6.69 (d, *J* = 8.0 Hz, 4 H, ArH), 6.58 (s, 2 H, pyrrole-H), 5.22 (s, 4 H, OCH_2), 4.31 (t, *J* = 6.8 Hz, 4 H, NCH_2), 4.17 (t, *J* = 4.0 Hz, 4 H, OCH_2), 3.87 (t, *J* = 4.4 Hz, 4 H, OCH_2), 3.77-3.73 (m, 4 H, OCH_2), 3.72-3.64 (m, 8 H, OCH_2), 3.55 (t, *J* = 4.0 Hz, 4 H, OCH_2), 3.38 (s, 6 H, OCH_3), 3.00 (s, 12 H, NCH_3), 1.92-1.84 (m, 4 H, CH_2), 1.46 (s, 6 H, CH_3), 1.43 (s, 6 H, CH_3), 1.37-1.31 (m, 4 H, CH_2); ^{13}C NMR (150.7 MHz, $CDCl_3$): δ = 160.09, 159.29, 158.70, 152.88, 150.99, 150.52, 145.76, 143.92, 143.64, 140.93, 139.21, 138.45, 136.53, 133.31, 130.18, 129.83, 129.36, 129.20, 128.48, 127.96, 125.17, 122.94, 122.84, 117.30, 116.87, 115.84, 115.37, 115.10, 115.00, 112.23, 82.81, 72.06, 70.99, 70.79, 70.71, 69.81, 67.67, 62.19, 62.14, 59.19, 50.26, 40.40, 30.15, 29.83, 25.95, 17.81, 14.94; HRMS (ESI): *m/z* calcd for $C_{96}H_{106}B_2F_4I_2N_{12}NaO_{10}$ $[M+Na]^+$, 1961.6259, found, 1961.6380.

4.2. Photo-physical and photo-chemical studies

4.2.1. GSH-responsive fluorescence emission

8a and **8b** were dissolved in DMF to obtain solutions with concentration of 1 mM, which were diluted to 10 μM with PBS containing 0.05% Tween 80. And then GSH was dissolved in PBS to obtain a 0.5 M GSH stock solution. To investigate the effect of GSH on the disulfide bond, we prepared a mixture of **8a** (10 μM) with GSH (2 μM and 10 mM) and **8b** (10 μM) with GSH (2 μM and 10 mM). All of these solutions were kept at room temperature during the test. And the fluorescence spectra ($\boldsymbol{\lambda_{ex}}$= 610 nm) of these solutions were recorded at different time intervals.

4.2.2. GSH-responsive singlet oxygen generation

In order to study the singlet oxygen generation efficiency, Firstly, 1 mM stock solution of 9,10-dimethylanthracence (DMA), 1 mM stock solution of compounds and the stock solution of GSH (0.5 M and 1 mM) were prepared in DMF. Then the mixture of **8a** (or **8b**) (10 μM) and DMA with GSH (2 μM and 10 mM) were prepared in PBS with 0.05% Tween 80, followed by illumination with light (670 nm, 20 $mW \cdot cm^{-2}$). The value were recorded by monitoring the decay of fluorescence intensity of DMA at 432 nm (λ_{ex}=370 nm).

4.3. In vitro studies

4.3.1. Intracellular fluorescence imaging, flow cytometry analysis and intracellular ROS measurements

HeLa, A549, H22 and HELF cells with a density of 10^5 cells in 1000 μL of DMEM were seeded in a confocal dish and incubated overnight at 37°C with 5% CO_2. Removing the medium and rinsing thrice with PBS. After that, replacing the medium with fresh DMEM containing GSH (5 mM, 1 mL). In addition, we set up a control group without GSH. Specifically, the cell culture medium (1 mL) was added under the same conditions, followed by incubation at 37 °C, 5% CO_2 for 2 h, and then the old medium was removed. After rinsing twice with PBS, **8a** (10 μM) or **8b** (10 μM) were added and cultured in a cell culture incubator for 8 h, and intracellular fluorescence was detected by laser confocal (excitation wavelength was 633 nm). And under the same conditions, the intracellular fluorescence intensity was measured by flow cytometry.

As for intracellular ROS measurements, after adding the compound and culturing for 12 h, we added DCFH-DA with DMEM and co-cultured for 1 h, rinsing with PBS for 5 times and then changing to serum-free, 1 mL without phenol red DMEM medium, the cells were irradiated with light at 670 nm (20 $mW \cdot cm^{-2}$) for 3 minutes, and intracellular fluorescence was detected by laser confocal scanning. ($\lambda_{ex} = 488$ nm for DCF green fluorescence and $\lambda_{ex} = 633$ nm for **8a**, **8b** red fluorescence, respectively). At the same time, in order to prove that the green fluorescence is caused by the ROS

generated by the photosensitizer, we added a set of pre-treated cells with VC (100 μM, 1 mL) (ROS scavenger) for 1 h and then added **8a**, **8b** stock solution. Intracellular fluorescence was detected by laser confocal microscopy under the same method.

4.3.2. Determination of intracellular GSH concentrations

HeLa, A549, H22 and HELF cells with a density of 2×10^6 cells in 10 mL of DMEM were seeded in a 96-well plates and incubated overnight at 37°C with 5% CO_2. After washed with phosphate buffer saline (PBS), lysed with 200 μL of cell lysates on ice and then were centrifuged (10000 × g) for 10 min at 4°C and the supernatant (10 μL) was mixed with 150 μL of the Glutathione Assay Kit. Then added 50 μL of 0.5 mg/mL NADPH solution and mixed well. The level of intracellular GSH was determined by recording the absorbance at 412 nm via a microplate reader 25 minutes later. And the protein concentration was then detected using a microplate reader with the BCA Protein Assay Kit. The final intracellular GSH concentration is expressed in nmol/mg-protein.

4.3.3. Photocytotoxicity studies

To study the cytotoxicity and photocytotoxicity, MTT assays against HeLa, A549, H22 and HELF cells were conducted. Approximately 6000 cells (100 μL) each well were seeded in 96-well plates and inoculated under 5% CO_2 overnight at 37°C. Then replacing the medium with fresh DMEM containing **8a** or **8b** (1% DMSO, 0.05% Tween 80) with different concentrations, respectively. After incubating for 24 h under dark conditions, treating the 96-well plates with light or not after replacing with fresh DMEM. For the irradiation group, the 96-well plates were irradiated with a 670 nm LED lamp for 2 minutes with a power of 20 $mW\cdot cm^{-2}$. Then the cells were inoculated at 37°C overnight under 5% CO_2. After that, the MTT (10 mL, 5 mg/mL) was added to per well and incubated for 4 h. Next, the DMEM was removed and added DMSO (100 μL) to each well. Finally, the OD values at 490 nm of each well were measured.

4.3.4. Subcellular localization

HeLa, A549, H22 and HELF cells with a density of 50000 cells in 1 mL of DMEM were seeded in a confocal dish and incubated overnight at 37°C with 5% CO_2. Then **8a**

(10 μM) or **8b** (10 μM) were added and cultured in a cell culture incubator for 12 h. DAPI, Lyso-Tracker Red and Mito-Tracker Green in the DMEM were added into the dish and incubated for minutes (DAPI: 20 min, Lyso-Tracker Red and Mito-Tracker Green are both 60 min). Subsequently, washed by PBS for 5 times and imaged. And the DAPI, Lyso-Tracker Red and Mito-Tracker Green were excited at 405 nm, 543 nm and 488 nm, and detected at 425-475 nm, 550-620 nm and 510-570 nm, respectively. And the compounds were excited at 633 nm and detected at 650-750 nm.

4.4. In vivo studies

Female KunMing mice (20-25 g) were purchased from the Laboratory Animal Services Centre of Wushi, Fuzhou, China. All animal experiments had been approved by the Animal Experimentation Ethics Committee of Fuzhou University. The mice were kept under pathogen-free conditions with free access to water and food. Selecting mice in good health and then H22 cells (10^7 cells/mL, 100 μL) were inoculated into the subcutaneous tissue on the back of the mice and when the average size of the tumor reached 50 mm^3, a series of experiments were carried out. For in vivo fluorescence imaging study, nine mice were randomly divided into three groups and treated with a single intravenous injection of saline, **8a** and **8b** (2 mg/kg, 200 μL), respectively. And collecting the whole body images at 0 h, 2 h, 6 h, 12 h and 24 h post-injection. And the mice were sacrificed at 24 h after injection to harvest the tumor and normal tissues, including heart, liver, spleen, lung, kidney for the ex vivo fluorescence images.

On the other hand, another 25 mice were randomly divided into five groups of five each and the mice were injected with saline, **8a** and **8b** (2 mg/kg, 100 μL) for three times on the first, fourth and seventh day respectively and then subjected to laser irradiation or not after 12 h of each administration: group 1 for saline (blank control), group 2 for **8a**, group 3 for **8a** with laser (670 nm, 100 mW/cm^2), group 4 for **8b**, group 5 for **8b** with laser (670 nm, 100 mW/cm^2). Monitoring the tumor volume and body weight every day for 15 days. Then the mice were sacrificed, then tumors were excised and weighed. For histological examination, tumors from all five groups and normal tissues (heart, liver, spleen, lung, and kidney) from group 4 and group 5 were harvested,

fixed overnight in 4% polyformaldehyde solution, embedded into paraffin, sectioned and stained with hematoxylin and eosin (H&E), and detected by digital microscopy.

Acknowledgments

This work was supported by the National Natural Science Foundation of China (project Nos. 21471033), the Key Project of Science and Technology Development of Fujian Province (project No. 2015Y0086), the Independent Research Project of State Key Laboratory of Photocatalysis on Energy and Environment (project Nos. 2014C04).

Appendix A. Supplementary data

Supplementary data to this article can be found online at https://doi.org/xxx.

Conflicts of interest

The authors declare no conflict of interest.

References

[1] D. E. J. G. J. Dolmans, D. Fukumura, R. K. Jain, Photodynamic therapy for cancer, Nat. Rev. Cancer 3 (2003) 380-387.

[2] A. P. Castano, P. Mroz, M. R. Hamblin, Photodynamic therapy and anti-tumour immunity, Nat. Rev. Cancer 6 (2006) 535-545.

[3] D. van Straten, V. Mashayekhi, H. S. de Bruijn, S. Oliveira, D. J. Robinson, Oncologic Photodynamic Therapy: Basic Principles, Current Clinical Status and Future Directions, Cancers 9 (2017) 10.3390/cancers9020019.

[4] K. Berg, P. Selbo, A. Weyergang, A. Dietze, L. Prasmickaite, A. Bonsted, B. Engesæter, E. Angell-Petersen, T. Warloe, N. Frandsen, A. Høgset, Porphyrin-related photosensitizers for cancer imaging and therapeutic applications, J. Microsc. 218 (2005) 133-147.

[5] J. F. Lovell, T. W. B. Liu, J. Chen, G. Zheng, Activatable Photosensitizers for Imaging and Therapy, Chem. Rev. 110 (2010) 2839-2857.

[6] B. Ghazal, E. N. Kaya, A. Husain, A. Ganesan, M. Durmuş, S. Makhseed, Biotinylated-cationic zinc(II) phthalocyanine towards photodynamic therapy, J. Porphyr. Phthalocya. 23 (2019) 46-55.

[7] K. Li, L. Qiu, Q. Liu, G. Lv, X. Zhao, S. Wang, J. Lin, Conjugate of biotin with silicon(IV) phthalocyanine for tumor-targeting photodynamic therapy, J. Photochem. Photobiol. B. 174 (2017).

[8] M. Yang, J. Deng, D. Guo, J. Zhang, L. Yang, F. Wu, A folate-conjugated platinum porphyrin complex as a new cancer-targeting photosensitizer for photodynamic therapy, Org. Biomol. Chem. 17 (2019) 5367-5374.

[9] M.-R. Ke, S.-L. Yeung, D. K. P. Ng, W.-P. Fong, P.-C. Lo, Preparation and in Vitro Photodynamic Activities of Folate-Conjugated Distyryl Boron Dipyrromethene Based Photosensitizers, J. Med. Chem. 56 (2013) 8475-8483.

[10] P. M. R. Pereira, W. Rizvi, N. V. S. D. K. Bhupathiraju, N. Berisha, R. Fernandes, J. P. C. Tomé, C. M. Drain, Carbon-1 versus Carbon-3 Linkage of D-Galactose to Porphyrins: Synthesis, Uptake, and Photodynamic Efficiency, Bioconjug. Chem. 29 (2018) 306-315.

[11] E. E. Kamarulzaman, A. M. Gazzali, S. Acherar, C. Frochot, M. Barberi-Heyob, C. Boura, P. Chaimbault, E. Sibille, H. A. Wahab, R. Vanderesse, New peptide-Conjugated Chlorin-Type Photosensitizer Targeting Neuropilin-1 for Anti-Vascular Targeted Photodynamic Therapy. Int. J. Mol. Sci. 16 (2015) 24059-24080.

[12] K. M. Harmatys, M. Overchuk, J. Chen, L. Ding, Y. Chen, M. G. Pomper, G. Zheng, Tuning Pharmacokinetics to Improve Tumor Accumulation of a Prostate-Specific Membrane Antigen-Targeted Phototheranostic Agent, Bioconjug. Chem. 29 (2018) 3746-3756.

[13] L. Zhu, J. Liu, G. Zhou, H. M. Ng, I. L. Ang, G. Ma, Y. Liu, S. Yang, F. Zhang, K. Miao, T. C. W. Poon, X. Zhang, Z. Yuan, C.-X. Deng, Q. Zhao, Targeting immune checkpoint B7-H3 antibody-chlorin e6 bioconjugates for spectroscopic photoacoustic imaging and photodynamic therapy, Chem. Commun. 55 (2019)14255-14258.

[14] F.-L. Zhang, M.-R. Song, G.-K. Yuan, H.-N. Ye, Y. Tian, M.-D. Huang, J.-P. Xue, Z.-H. Zhang, J.-Y. Liu, A Molecular Combo of Zinc(II) Phthalocyanine and Tamoxifen Derivative for Dual Targeting Photodynamic Therapy and Hormone Therapy, J. Med. Chem. 60 (2017) 6693-6703.

[15] H. He, S. Ji, Y. He, A. Zhu, Y. Zou, Y. Deng, H. Ke, H. Yang, Y. Zhao, Z. Guo, H. Chen, Photoconversion-tunable fluorophore vesicles for wavelength-dependent photo-induced cancer therapy, Adv Mater. 27 (2017), 1606690.

[16] W. Hu, H. Ma, B. Hou, H. Zhao, Y. Ji, R. Jiang, X. Hu, X. Lu, L. Zhang, Y. Tang, Q. Fan, W. Huang, Engineering Lysosome-Targeting BODIPY Nanoparticles for Photoacoustic Imaging and Photodynamic Therapy under Near-Infrared Light, ACS Appl. Mater. Inter. 8 (2016) 12039-12047.

[17] X. Li, S. Kolemen, J. Yoon, E. U. Akkaya, Activatable Photosensitizers: Agents for Selective Photodynamic Therapy, Adv. Funct. Mater. 27 (2017) 1604053.

[18] M. Gangopadhyay, R. Mengji, A. Paul, Y. Venkatesh, V. Vangala, A. Jana, N. D. P. Singh, Redox-responsive xanthene-coumarin-chlorambucil-based FRET-guided theranostics for "activatable" combination therapy with real-time monitoring, Chem. Commun. 53 (2017) 9109-9112.

[19] Q. Wang, L. Yu, R. C. H. Wong, P.-C. Lo, Construction of cathepsin B-responsive fluorescent probe and photosensitizer using a ferrocenyl boron dipyrromethene dark quencher, Eur. Med. Chem. 179 (2019) 828-836.

[20] N. Gharibi, K. Kailass, A. A. Beharry, Exploiting the Cellular Redox-Control System for Activatable Photodynamic Therapy, ChemBioChem 20 (2019) 345-349.

[21] Z. Li, Y. Liu, L. Chen, X. Hu, Z. Xie, A glutathione-activatable photodynamic and fluorescent imaging monochromatic photosensitizer, J. Mater. Chem. B 5 (2017) 4239-4245.

[22] J. Tian, L. Ding, H.-J. Xu, Z. Shen, H. Ju, L. Jia, L. Bao, J.-S. Yu, Cell-Specific and pH-Activatable Rubyrin-Loaded Nanoparticles for Highly Selective Near-Infrared Photodynamic Therapy against Cancer, J. Am. Chem. Soc. 135 (2013) 18850-18858.

[23] H. Xiong, K. Zhou, Y. Yan, J. B. Miller, D. J. Siegwart, Tumor-Activated Water-Soluble Photosensitizers for Near-Infrared Photodynamic Cancer Therapy, ACS Appl. Mater. Inter. 10 (2018) 16335-16343.

[24] Z.-W. Wang, D. Su, X.-Q. Li, J.-J. Cao, D.-C. Yang, J.-Y. Liu, A H_2O_2-Responsive Boron Dipyrromethene-Based Photosensitizer for Imaging-Guided Photodynamic Therapy, Molecules 24

(2019) 32.

[25] M. R. Ke, D. K. P. Ng, P. C. Lo, A pH-responsive fluorescent probe and photosensitiser based on a self-quenched phthalocyanine dimer, Chem. Commun. 48 (2012) 9065-9067.

[26] S. Alpugan, D. Topkaya, F. Dumoulin, Disulfide-bridge dimeric porphyrin and their reference compounds for glutathione-based specific tumor-activation, J. Porphyr. Phthalocya. 21 (2018) 918-924.

[27] W. Piao, K. Hanaoka, T. Fujisawa, S. Takeuchi, T. Komatsu, T. Ueno, T. Terai, T. Tahara, T. Nagano, Y. Urano, Development of an Azo-Based Photosensitizer Activated under Mild Hypoxia for Photodynamic Therapy, J. Am. Chem. Soc. 139 (2017) 13713-13719.

[28] J.-N. Liu, W. Bu, J. Shi, Chemical Design and Synthesis of Functionalized Probes for Imaging and Treating Tumor Hypoxia, Chem. Rev. 117 (2017) 6160-6224.

[29] W. Wang, G. Liang, W. Zhang, D. Xing, X. Hu, Cascade-Promoted Photo-Chemotherapy against Resistant Cancers by Enzyme-Responsive Polyprodrug Nanoplatforms, Chem. Mater. 30 (2018) 3486-3498.

[30] M. Chiba, Y. Ichikawa, M. Kamiya, T. Komatsu, T. Ueno, K. Hanaoka, T. Nagano, N. Lange, Y. Urano, An Activatable Photosensitizer Targeted to gamma-Glutamyltranspeptidase, Angew. Chem. Int. Ed. 56 (2017) 10418-10422.

[31] F. Xue, P. Wei, X. Ge, Y. Zhong, C. Cao, D. Yu, T. Yi, A pH-responsive organic photosensitizer specifically activated by cancer lysosomes, Dyes Pigm. 156 (2018) 285-290.

[32] H. Horiuchi, R. Kuribara, A. Hirabara, T. Okutsu, pH-Response Optimization of Amino-Substituted Tetraphenylporphyrin Derivatives as pH-Activatable Photosensitizers, J. Phys. Chem. A 120 (2016) 5554-5561.

[33] F. Yuan, J. L. Li, H. Cheng, X. Zeng, X. Z. Zhang, A redox-responsive mesoporous silica based nanoplatform for in vitro tumor-specific fluorescence imaging and enhanced photodynamic therapy, Biomater. Sci. 6 (2017) 96-100.

[34] B. Chen, W. Dai, B. He, H. Zhang, X. Wang, Y. Wang, Q. Zhang, Current Multistage Drug Delivery Systems Based on the Tumor Microenvironment, Theranostics 7 (2017) 538-558.

[35] M. P. Gamcsik, M. S. Kasibhatla, S. D. Teeter, O. M. Colvin, Glutathione levels in human tumors, Biomarkers 17 (2012) 671-691.

[36] K. Li, W. Dong, L. Qiu, Q. Liu, G. Lv, Y. Peng, M. Xie, J. Lin, A new GSH-responsive prodrug of 5-aminolevulinic acid for photodiagnosis and photodynamic therapy of tumors, Eur. J. Med. Chem. 181 (2019) 111582.

[37] I. S. Turan, F. P. Cakmak, D. C. Yildirim, R. Cetin-Atalay, E. U. Akkaya, Near-IR absorbing BODIPY derivatives as glutathione-activated photosensitizers for selective photodynamic action, Chem. Eur. J. 20 (2014) 16088-16092.

[38] S. Erbas-Cakmak, F. P. Cakmak, S. D. Topel, T. B. Uyar, E. U. Akkaya, Selective photosensitization through an AND logic response: optimization of the pH and glutathione response of activatable photosensitizers, Chem. Commun. 51 (2015) 12258-12261.

[39] H. He, P.-C. Lo, D. K. P. Ng, A Glutathione-Activated Phthalocyanine-Based Photosensitizer for Photodynamic Therapy, Chem. Eur. J. 20 (2014) 6241-6245.

[40] A. Kamkaew, S. H. Lim, H. B. Lee, L. V. Kiew, L. Y. Chung, K. Burgess, BODIPY dyes in photodynamic therapy, Chem. Soc. Rev. 42 (2013) 77-88.

[41] S. Kolemen, E. U. Akkaya, Reaction-based BODIPY probes for selective bio-imaging, Coordination Chem. Rev. 354 (2018) 121-134.

[42] H. Lu, J. Mack, Y. Yang, Z. Shen, Structural modification strategies for the rational design of red/NIR region BODIPYs, Chem. Soc. Rev. 43 (2014) 4778-4823.

[43] W. J. Shi, P. C. Lo, S. Zhao, R. C. Wong, Q. Wang, W. P. Fong, D. K. Ng, A biotin-conjugated glutathione-responsive FRET-based fluorescent probe with a ferrocenyl BODIPY as the dark quencher, Dalton T. 45 (2016) 17798-17806.

[44] S. Çetindere, S. O. Tümay, A. Kılıç, M. Durmuş, S. Yeşilot, Synthesis and physico-chemical properties of cyclotriphosphazene-BODIPY conjugates, Dyes Pigm. 139 (2017) 517-523.

[45] M.D. Maree, N. Kuznetsova, T. Nyokong, Silicon octaphenoxyphthalocyanines: Photostability and singlet oxygen quantum yields. J. Photochem. Photobiol. A 140 (2001) 117–125.

Highlights:

1. A novel glutathione-responsive photosensitizer has been synthesized.
2. The photosensitizer can be activated by glutathione in solution and cancer cells.
3. The photosensitizer exhibits a high photodynamic activity to cancer cells.
4. The photosensitizer can be efficiently accumulated and activated in tumor.
5. The photosensitizer shows a strong inhibition on tumor growth.

Declaration of interests

☒ The authors declare that they have no known competing financial interests or personal relationships that could have appeared to influence the work reported in this paper.

☐The authors declare the following financial interests/personal relationships which may be considered as potential competing interests: